Engineering Science and Technology, an International Journal 24 (2021) 728–735

HOSTED BY

Contents lists available at ScienceDirect

Engineering Science and Technology, an International Journal

journal homepage: www.elsevier.com/locate/jestch

Full Length Article

A numerical investigation on the through rib stiffener beam to concrete-filled steel tube column connections subjected to cyclic loading

M. Ansari [a,*], M.Z Jeddi [b], W.H.W. Badaruzzaman [a,*], M.M. Tahir [c], S.A. Osman [a], E. Hosseinpour [a]

[a] Department of Civil Engineering, Universiti Kebangsaan Malaysia, UKM, 43600 Bangi, Selangor, Malaysia
[b] Department of Civil Engineering, Faculty of Engineering, University of Malaya, 50603 Kuala Lumpur, Malaysia
[c] UTM Construction Research Centre, Faculty of Civil Engineering, Institute for Smart Infrastructure and Innovative Construction, UTM, 81310 Johor Bahru, Johor, Malaysia

ARTICLE INFO

Article history:
Received 17 April 2020
Revised 6 September 2020
Accepted 13 October 2020
Available online 6 November 2020

Keyword:
Through rib stiffener
CFT column
Beam-to-column connection
Cyclic loading
FE analysis

ABSTRACT

This research presents a numerical investigation on the behaviour of through rib stiffener steel beam connected to circular concrete-filled steel tube (CFT) column subjected to the cyclic loading. A nonlinear Finite Element (FE) model was established using ABAQUS/Standard program. The accuracy of the FE result was examined through comparing it with the previous experimental test results. The effects of various parameters on the failure mode and ultimate moment capacity of the connections were investigated on twenty-four FE models. The parameters were stiffener' height, length, and thickness including varied thicknesses and diameters of the hollow circular steel tube. The FE results indicated that the larger height of the through rib stiffener improved buckling behaviour of the steel tube column and the moment capacity by 8%. Meanwhile, the longer and thicker through rib stiffener effectively shifted the beam plastic hinge's location away from the column, which resulted in 4% improvement in ultimate moment capacity of the connection.

1. Introduction

Concrete-filled tubular (CFT) columns are generally more preferred than the reinforced concrete (RC) and steel columns because of their several advantages such as higher strength, ductility, and stiffness. The connection of CFT column to steel beams for moment-resisting frame is always more crucial compared to the conventional steel and RC columns. Previous studies conducted on the CFT column connection revealed that direct welding or bolting of the steel beam to the column tube might compromise the lateral confinement pressure of the steel tube to the infilled concrete [1]. Therefore, the steel beam connection to CFT column has been examined through various bolting and welding methods [1–10]. A review study was conducted by Zhichao et al. [11] discussed the experimental results of the steel beam connection to the CFT column. The "Through beam" method has been found the most suitable connection in terms of the moment-resisting frame due to its high strength, stiffness, and ductility [12,13]. This connection allows a beam to pass through the pre-slotted steel tube where the entire perimeter of the beam section at the connecting part is welded to the steel tube surface.

For decades, several experimental and analytical studies have investigated the behavior of through beam connection. For example, an experimental study was conducted by Elremaily and Azizinamini [14]. Seven specimens in two-third scale of through beam connection were designed in a way to distinguish possible distinct modes of failure and estimate the joint shear strength. The test parameters were the column-to-beam moment capacity ratio, varied welding types on beams to the tube connection, and the connection elements within the panel zone. The failures were observed at column and beam including the joint itself. The column-to-beam moment capacity ratio less than or around one lead to column failure, while the strong column-weak beam criterion leads to the beam failures as beam plastic hinges form in the vicinity of the connection. The experimental results of this study were used by Arabnejad et al. [15] to validate seven finite element models. That numerical study investigated the effect of different axial load levels (0, 0.2, 0.4, and 0.6), including the boundary condition of the through beam connections. The finite element results confirmed the failure due to formation of plastic hinge in the beams where the plastic moment of the beam was achieved in different axial load levels. In addition, the shear failure was found at the beam-column joint with no noticeable effect of the axial load level on the shear capacity.

* Corresponding author.
E-mail addresses: ansari6127@siswa.ukm.edu.my (M. Ansari), wanhamidon@ukm.edu.my (W.H.W. Badaruzzaman).

Peer review under responsibility of Karabuk University.

https://doi.org/10.1016/j.jestch.2020.10.004
2215-0986/

Accordingly, through rib stiffener beam connection is an innovative form of the though beam connection, was proposed by Jeddi et al. [12] where the steel beam' flanges were reinforced by two vertical rib stiffener plates at the vicinity of the joint. The cyclic behavior of the proposed connection was tested experimentally, and the two through rib stiffener beam connection specimens were examined with corresponding conventional through beam connection specimens. The CFT column properties of all specimens were same; thus, two different sizes were selected for main beam and orthogonal beam for each through rib stiffener connection. The result indicated better performance of the through rib stiffener beam connection in terms of ductility, rigidity, energy dissipation, and moment capacity. The plastic hinge was formed at the main beams in all tested specimens. However, in though rib stiffener connections, the plastic hinges were formed at the tip of the rib stiffeners in beam and at the surface of the columns. A higher moment capacity of the connections was recorded using the rib stiffeners, where the plastic hinges were closer to the free end of the beams. In addition, the rib stiffeners enhanced the steel tube strength as the local buckling of steel tube occurred in the through beam connection specimen.

Meanwhile, no local buckling was seen on the steel tube of the corresponding specimens with through rib stiffener connection.

The experimental results showed that the rib stiffener improves the strength of the connection together with the column. However, due to limited tests, more studies are required to fully evaluate the behavior of the through rib stiffener beam connections and their failure modes. Thus, this numerical study aims to investigate the ultimate moment of the connection and its failure modes under cyclic loading. To this end, the geometry of the rib stiffener and different flexural capacity ratios of the column-to-beam connection need to be examined.

2. Overview of the experimental program

In this study, the experimental results and the specifications of the through rib stiffener beam specimen labeled as TOBC4 reported by Jeddi et al. [12] were used to establish the Finite Element (FE) model. In the test specimen, the main beam's web and flanges were reinforced by welding the rib and web stiffener plates, then the reinforced main beam and the orthogonal beam were passed though the steel column and joined to the steel column by full penetration welding. Afterward, the steel tube was filled with concrete. Fig. 1 shows the details of the test specimen. The lengths of the column and the beams were 1920 mm and 3000 mm, respectively.

Fig. 2 shows the boundary condition and loading of the test specimen. The top and bottom of the column were restrained by a roller and hinge supports, respectively, which restrained the column from the horizontal translations (in direction of X and Z-axis) as well as rotation in Y and Z-axis. In addition, the main beam was

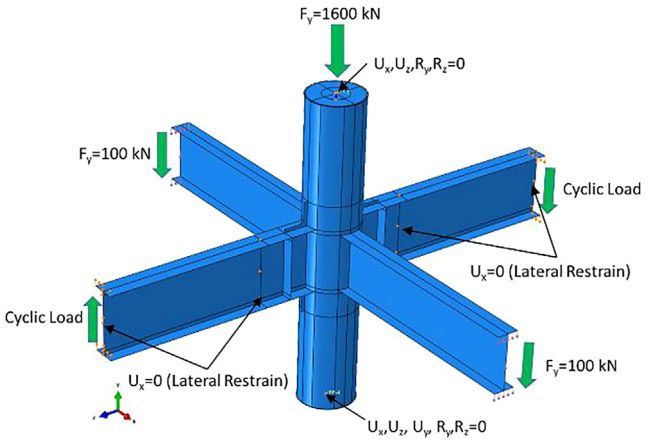

Fig. 2. The boundary condition and loading.

laterally restrained at the main beam free ends and 1 m from the beam free ends. The specimen was loaded in 2 steps, in which, the column and the orthogonal beam ends were pre-loaded by 1600 kN and 100 kN vertical loads at step 1, respectively, and maintained during the test. At step 2, two cyclic loads in opposite directions were subjected to the main beam free ends. The vertical loads subjected to the column and orthogonal beam ends simulated the gravity loads in multistory building. The total amount of the loads was considered as 25% of the squash load of the CFT column, to satisfy the design limitation of the thorough beam connection proposed by Elremaily and Azizinamini [14].

3. Finite element modeling

3.1. General

To study the performance of the through-rib stiffener beam-to-CFT column connection under cyclic loading, a nonlinear model was established using ABAQUS/Standard program. The geometric and material nonlinearities were considered in the analysis to obtain the nonlinear behavior and the probable buckling of the model. Since instantaneous loading is not available in ABAQUS/Standard, two steps were defined to apply the loadings. Similar to the experimental program, the column and orthogonal beam were loaded at the first step and the loads were kept constant during the second step. The cyclic loading was performed at the second step. The period of each load cycle was set to 4 s, with 1 s for each phase of the cyclic load. The initial and maximum phases of the step 2 was set to 0.1 s to have equal and smooth increments during analysis. Moreover, the automatic incrimination was considered in this step to minimize the convergence problems.

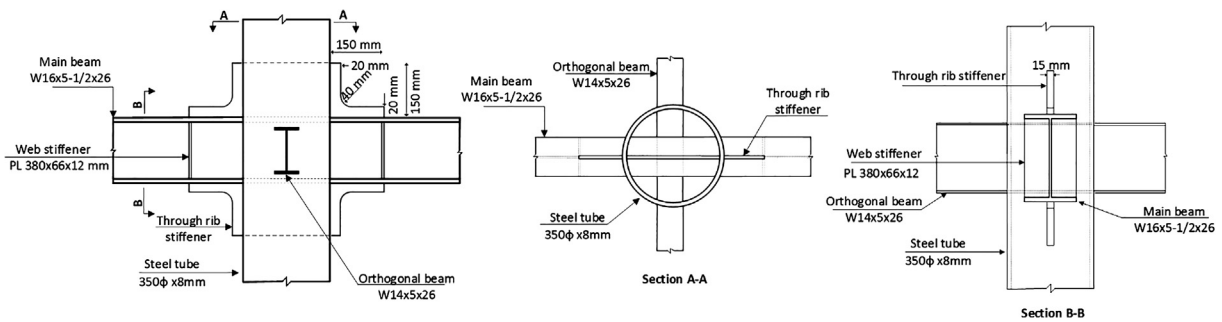

Fig. 1. The details of test specimen (TOBC4).

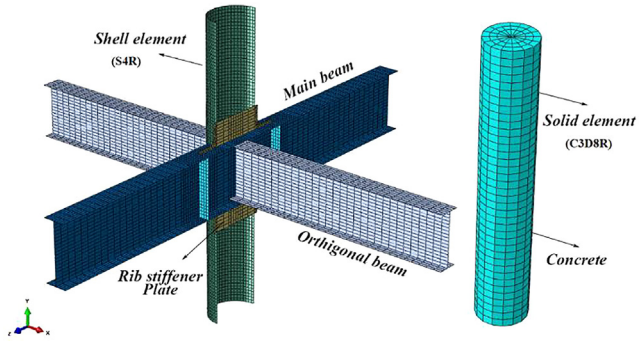

Fig. 3. The FE model elements and meshes.

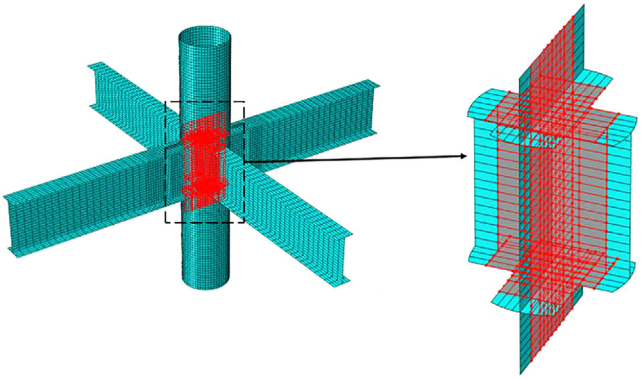

Fig. 4. The FE model elements and meshes.

3.2. Element types and mesh

The components and the mesh used in the FE model are shown in Fig. 3. The optimum element sizes were obtained from convergence study. Moreover, hourglass control and reduced integration were selected for the element. The steel elements were modeled by four-node shell element (S4R) except the outer parts of the through-rib stiffener plate, which were modelled with a 3-node triangular shell element (S3) due to the curved edges. A fine mesh with the size of 20 mm was used for the steel tube and the parts of main beam with high risk zone. Whereas, the other parts were modeled by a coarse mesh with the size of 60 mm to save the analysis time. The infill concrete was modeled using an 8-node solid element (C3D8R) with the element size of 50 mm. This element was a general-purposed brick element with reduced integration, which has been adopted for concrete material in recent studies [15–17].

3.3. Surface interaction

The steel components were merged at connection point to eliminate weld modelling and complexity of interactions. The interaction between the concrete core and inner surface of steel tube was modeled using the node-to-surface contact. Hard contact and penalty mode with a friction coefficient of 0.6 were adopted for the properties of the contact in the normal and tangential directions, respectively, which have been suggested in previous studies [18,19].

The through beams inside the concrete core act as shear connector for each other. Since the beam area was too big as shear connector, full bond between concrete and the through beams was considered. Therefore, the nodes of orthogonal and stiffened main beam inside the concrete core were embedded within the concrete infill elements. It should be noted that the nodes of through beams at the surface of the steel tube, which had also contact interaction with the concrete core, were eliminated from the node set to avoid error in the analysis. Fig. 4 demonstrates the embedded nodes of the orthogonal and stiffened main beams, which are highlighted by red color.

3.4. Material modeling

The stress–strain relationship of the steel materials was simulated by an isotropic bilinear model. The Flow and Von Mises rules were utilized to define the plastic deformation and yield surface of the materials, respectively. Table 1 presents the yield stress, ultimate stress, and the elongation of the steel materials obtained from the experimental test [12]. Modulus of elasticity and Poisson's ratio of the steel components are 199 GPa and 0.3, respectively.

The concrete damage plasticity option available in ABAQUS was used for the plastic behavior of the confined concrete material. This option can simulate crushing and cracking of the concrete in compression and tension, respectively. In addition, the elastic behavior of the concrete material was defined using elastic-isotropic option. The Poisson's ratio of the concrete material is 0.2 and the modules of elasticity (E_c) was determined using Eq. (1). The compressive strength (f'_c) was 70.1 MPa, as reported in the test [12]. The compressive and tensile stress–strain relationship of the concrete material were simulated using Eqs. (2) and (3), respectively [20,21].

$$E = 9.5(f'_c + 8)^{1/3} \tag{1}$$

$$\sigma_c = \left(\frac{kn - kn^2}{1 + (k-2)n}\right) f'_c \tag{2}$$

where $k = 1.16E\frac{\varepsilon_0}{f'_c}$ and $n = \frac{\varepsilon_c}{\varepsilon_0}$, ε_c and σ_c are the compressive stress and strain of the concrete, respectively, and ε_0 is the strain at the maximum compressive stress (f'_c), which is equal to 0.0022 [15]. The failure strain of concrete equals to 0.0035 [21].

$$\sigma_t = \begin{cases} E\varepsilon_t : \varepsilon_t \leqslant \varepsilon_{cr} \\ f_{cr}\left(\frac{\varepsilon_{cr}}{\varepsilon_t}\right)^{0.4} : \varepsilon_t > \varepsilon_{cr} \end{cases} \tag{3}$$

Table 1
Material properties of steel components.

Component	Yield Stress (MPa)	Ultimate Stress (MPa)	Elongation (%)
W 16 × 5–1/2 × 26	288.47 (F)	426.50 (F)	28.60 (F)
	291.31 (W)	426.75 (W)	26.76 (W)
W 14 × 5 × 26	313.55 (F)	446.18 (F)	27.44 (F)
	380.68 (W)	453.87 (W)	22.60 (W)
Steel tube	340.22	494.89	24.04
Through-rib stiffener	331.5	478.50	26.30
Web stiffener	331.5	478.50	26.30

The letters F and W stand for flange and web, respectively.

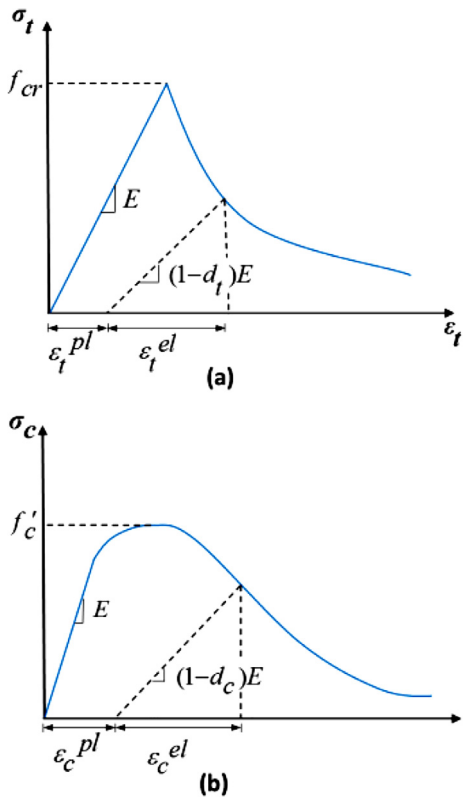

Fig. 5. The typical stress–strain relationship of the concrete a) in tension b) in compression.

where $f_{cr} = 0.31\sqrt{f'_c}$ and $\varepsilon_{cr} = \frac{f_{cr}}{E}$, ε_t and σ_t are the tensile stress and tensile strain of the concrete, respectively, and f_{cr} and ε_{cr} are concrete crack stress and concrete crack strain, respectively.

Fig. 5 shows typical tensile and compressive strain–stress relationships of the concrete material. It shows that the elastic stiffness of the concrete material degraded in the softening section of the stress–strain curves. The degradation of the concrete elastic stiffness is simulated using damage parameters in compression (d_c) and tension (d_t) available in concrete damage plasticity option. Since cyclic loading was applied to the FE model, the degradation of the concrete elastic stiffness was considered for the unloading process. The damage parameters in compression (d_c) and tension (d_t) were calculated using Eqs. (4) and (5) [22]. Furthermore, the default values of the stiffness recovery coefficient in compression (w_c) and tension (w_t) were considered in the concrete damage option.

$$d_c = 1 - \frac{\sigma_c}{E(\varepsilon_c - \varepsilon_p)} \tag{4}$$

$$d_t = 1 - \frac{\varepsilon_{cr}}{\varepsilon_t} \tag{5}$$

where ε_p is the concrete plastic strain in compression. The other concrete damage plasticity parameters were adopted based on previous studies, as presented in Table 2 [19].

3.5. Boundary conditions and loading

The loading and boundary conditions of the FE model were the same as the experimental test setup, as discussed earlier. To apply the boundary conditions and axial load to the column, two reference points were tied to the columns ends area using the rigid body option available in ABAQUS [22]. The reference points at the column ends can distribute uniformly the load to all nodes of the column ends. To model the hinge and roller supports at the column ends, the rotational movement were freed about X-axis (in the loading plane) at the columns ends. The translational movement in Y-direction was also freed (in the direction of axial load) at the top of the column end, while the other translational and rotational movements were restrained. In addition, a point load with magnitude of 1600 kN was applied to the top reference point as axial load. The lateral supports of the main beam were simulated by restraining the beam web nodes against lateral movement (X-axis) at the same locations of the tested beam. In order to apply the orthogonal preloads, uniformly-distributed shear loads were subjected to the cross-sectional area of the orthogonal beam ends.

Two vertical displacements (Y-direction) with tabular amplitude in opposite directions were subjected to the cross-sectional surface of the main beam ends to resemble the displacement control cyclic loading of the experimental test. Fig. 6 shows the cyclic loading sequences applied to the FE model.

3.6. FE model verification

The FE model was then verified with the experimental test results. The experimental results of TOBC4, including the failure type and the moment-rotation result, were used in this comparison. Fig. 7 compares the moment-rotation hysteresis loops obtained from FE analysis and the experimental test, which match each other well. The maximum moment of the FE result in the positive and negative directions were 273.98 kN.m and 269.63 kN.m, respectively, which were 2.94% and 11.85% lower than the experimental results in the positive and negative directions, respectively. The differences between the moments of FE and experimental after ultimate moment is related to the failure mechanism of the steel material that has not been defined in the model, which caused an overestimation in the FE result after ultimate moment The comparison of the results illustrated a reasonable accuracy of the FE analysis in terms of the moment-rotation curve.

The failure type of the FE model was compared with the experimental test presented in Fig. 8. The beam plastic hinges at the tip of rib stiffener plates are observed in both FE result and the experimental. It can be also observed that the web and flanges buckling of the main beam in both FE model and test specimen are quite similar. Thus, the FE model fairly represented the cyclic behavior and failure type of the through rib stiffener connection.

4. Parametric studies

A total of 24 FE models were developed to study the effect of the column-to-beam moment capacity ratio and the rib stiffener' geometry, including the height (h_s), thickness (t_s), and the length (L_s) of the through stiffener plate on the failure mode and ultimate moment of the through rib stiffener beam connection. Table 3

Table 2
The value of concrete damage plasticity parameters.

Dilatation angle	Eccentricity	fb_0 / fc_0	K	Viscosity
40	0.1	1.16	0.67	0.0001

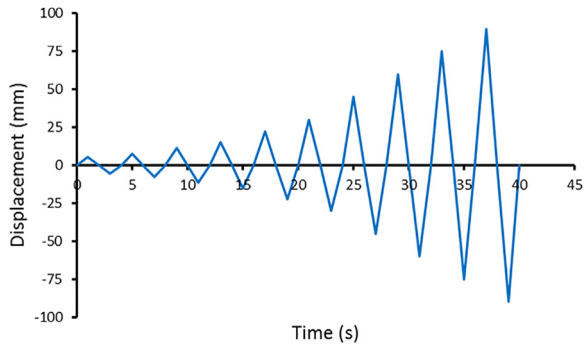

Fig. 6. The cyclic loading sequences.

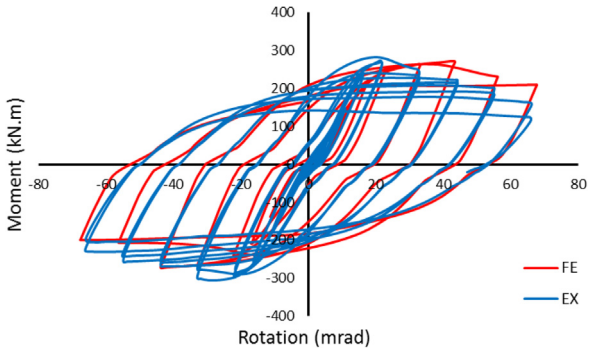

Fig. 7. Comparison of the moment-rotation curve of the experimental and FE analysis.

presents the details of the FE models. To investigate the effect of each parameter, the FE models were grouped as follow:

Group 1 includes FEM-R and FEM-1 to FEM-10, which investigated the influence of column-to-beam moment capacity ratio (r) on the failure type and ultimate moment of the connection. The ratio (r) of the models varied from 0.85 to 1.67, as presented in Table 3. Since the only failure type observed in the experimental test was beam failure, the ratios (r) selected for the FE models were lower than the tested specimen to find the other possible failure types. This reduction was done by decreasing the CFT column capacity, while the beams' sections remained as the test specimen. The column diameter (d_c), steel tube thickness (t_t), concrete compressive strength (f'_c), and axial load-to-nominal pure axial capacity ratio (P/P_0) were selected as the effective parameters on the CFT column moment capacity. The moment capacity and nominal pure axial capacity of the CFT columns were determined in accordance with AISC specifications (2010) [23]. The column to beam flexural strength ratio (r) were calculated as summation of the moment capacity of the CFT columns below and above the joint over the summation of the moment capacity of the main beams (the stiffeners excluded in the moment capacity) [13].

Group 2 studies the influence of the through rib stiffener height (h_s) using FEM-R, FEM-1, FEM-9 and FEM-11 to FEM-17. Four different through rib stiffener heights including 80 mm, 150 mm, 200 mm, and 280 mm were used in these models.

Group 3 investigates the effect of the through rib stiffener thickness (t_s), which includes FEM-R, FEM-10, FEM-15, and FEM-18 to FEM-21. Three different through rib stiffener thickness, i.e., 8 mm, 10 mm, and 15 mm were considered in this investigation.

Group 4 studies the influence of the through stiffener length (Ls), which includes FEM-R, FEM-10, FEM-22, and FEM-23. Three different through rib stiffener lengths, i.e., 100 mm, 150 mm, and 250 mm were used. L_s is considered as the length of through rib stiffener out of the column, which is equal to 150 mm for TOBC 4, as shown in Fig. 1.

4.1. Effect of the column-to-beam moment capacity ratio

Fig. 9 compares the moment-rotation envelope curves of the models in Group 1. The results show that the column-to-beam moment capacity ratio did not considerably affect the ultimate moment of the connections. The result showed only 3% difference in the ultimate moments of FEM-8 and FEM-R, which had the lowest and highest column-to-beam moment capacity ratio, respectively. The low difference between the ultimate moments is because all models' main beams achieved their plastic moment capacities.

According to the results, the plastic hinges were observed at the vicinity of through rib stiffeners in all models' main beams. In addition to the plastic hinges in the main beams of FEM-8 and FEM-9, Fig. 10 shows that the local buckling on the steel tubes of the models occurred right after the rib stiffener plates. The failure type of the other models was similar to that of FEM-R.

4.2. Effect of through rib stiffener height

Fig. 11 compares the moment-rotation envelopes of the models in Group 2. In this group, the models with the same column-to-beam moment capacity ratio were compared with each other. The comparison of the ultimate moment of FEM-R and FEM-11 showed that reducing the through rib stiffener height from

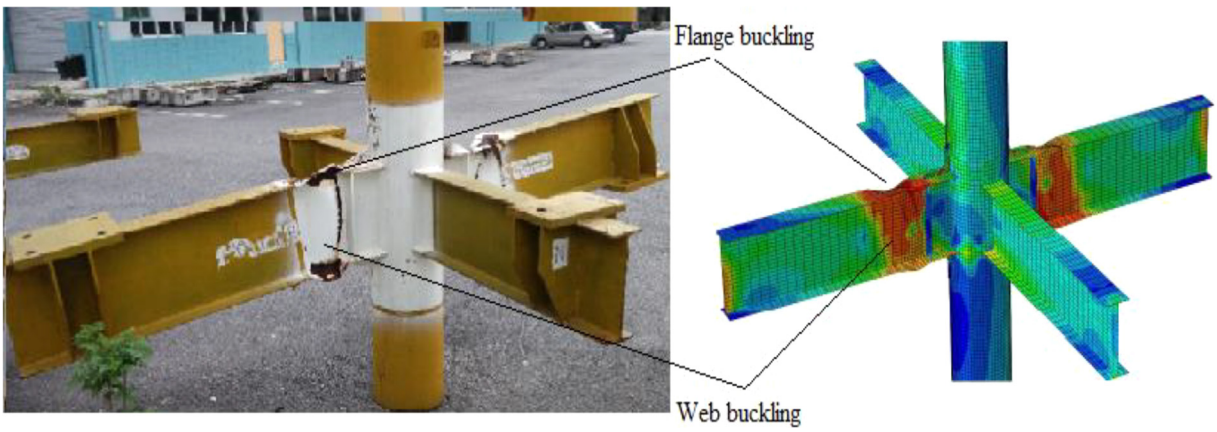

Fig. 8. Comparison of the failure mode of the experimental and FE analysis.

Table 3
The details of the FE models.

Model ID	f'_c (Mpa)	d_c (mm)	t_t (mm)	h_s (mm)	t_s (mm)	L_s (mm)	P/P_0 (%)	R	$+M_u$ (kN.m)	$-M_u$ (kN.m)
FEM-R	70	350	8	150	15	150	20	1.67	273.6	−268.7
FEM-1	70	350	4	150	15	150	20	1.10	269.4	−269
FEM-2	50	350	8	150	15	150	20	1.53	272.0	−271.8
FEM-3	40	350	8	150	15	150	20	1.47	272.2	−269.9
FEM-4	30	350	8	150	15	150	20	1.40	272.6	−268.8
FEM-5	30	350	6	150	15	150	20	1.12	273.7	−269.2
FEM-6	30	350	8	150	15	150	30	1.32	271.5	−271.4
FEM-7	30	350	8	150	15	150	40	1.10	271.5	−271.5
FEM-8	30	350	8	150	15	150	50	0.85	266.3	−271.3
FEM-9	70	286	8	150	15	150	20	1.02	264.8	−259.1
FEM-10	70	286	10	150	15	150	20	1.19	269.9	−269.7
FEM-11	70	350	8	80	15	150	20	1.67	269.6	−269.4
FEM-12	70	350	4	80	15	150	20	1.10	266.6	−228.6
FEM-13	70	286	8	80	15	150	20	1.02	253.9	−247.2
FEM-14	70	286	8	200	15	150	20	1.02	268.2	−262.4
FEM-15	70	286	8	280	15	150	20	1.02	268.3	−266.1
FEM-16	70	286	4	280	15	150	20	0.67	251.3	−265.7
FEM-17	70	286	6	280	15	150	20	0.85	268.4	−255.5
FEM-18	70	350	8	150	8	150	20	1.67	261.8	−260.8
FEM-19	70	286	8	280	8	150	20	1.02	267.2	−264.6
FEM-20	70	286	8	280	10	150	20	1.02	268.6	−263.8
FEM-21	70	286	10	150	8	150	20	1.19	266.8	−262.8
FEM-22	70	350	8	150	15	250	20	1.67	281.5	−279.8
FEM-23	70	286	10	150	8	100	20	1.19	263.4	−258.0

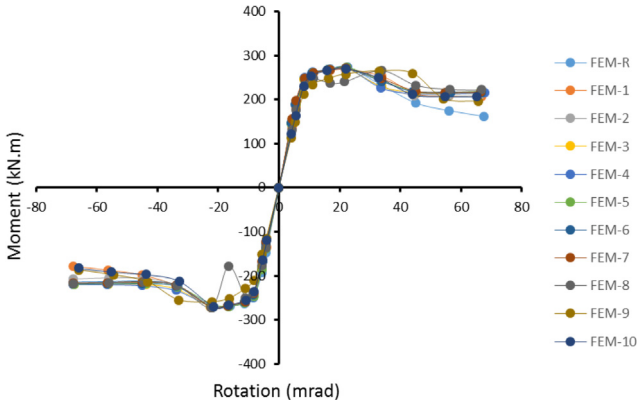

Fig. 9. The moment-rotation envelope curves of Group 1.

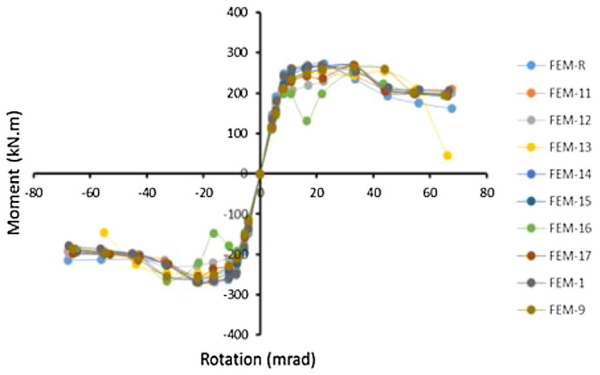

Fig. 11. The moment-rotation envelope curves of Group 2.

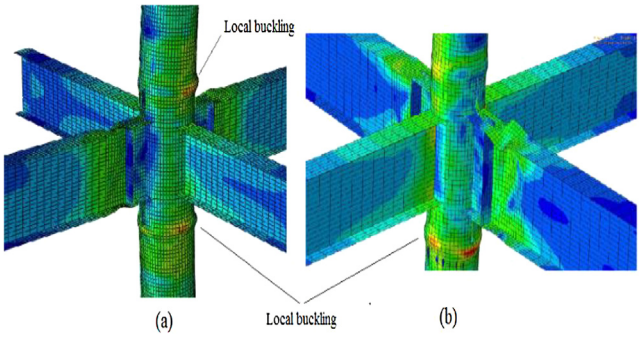

Fig. 10. The failure mode of (a) FEM-9 (b) FEM-8.

150 mm to 80 mm decreased the ultimate moment of FEM-11 by only 2%.

Fig. 12a also shows that failure type of FEM-11 was similar to that of FEM-R despite the difference in their though rib stiffener heights. On the other hand, FEM-12 gained 12% less ultimate moment compared to FEM-1, which was due to the same reduction in though rib stiffener height. Additionally, the steel tube of FEM-12 buckled locally right after the rib stiffener plates as a result of reducing the through rib stiffener height from 150 mm to 80 mm, as shown in Fig. 12b.

The comparison of the results of FEM-9, FEM-13, FEM-14, and FEM-15 shows that increasing the through rib stiffener from 80 mm to 280 mm improves the ultimate moment capacity of the connection by approximately 8%. Fig. 11 shows FEM-13 (hs = 80 mm) has a brittle behavior as the model, unlike the others, failed at lower rotation in the negative direction. Fig. 12c shows that the failure of FEM-13 was severe local buckling of the steel tube and unlike the other models without formation of plastic hinges at its main beam. Furthermore, Fig. 12d and e show that increasing the height of the through rib stiffener prevented the local buckling of the steel of FEM-14 and FEM-15.

The ultimate moments of FEM-16 and FEM-17 were also 8% higher than FEM-13, despite the thinner steel tube used in FEM-16 and FEM-17 (4 mm and 6 mm, respectively). This shows that deeper through rib stiffener improves the ultimate moment of the connection. The local buckling of the steel tubes and the beams plastic hinge were the failure types of FEM-16 and FEM-17, as depicted in Fig. 12f and 12g, respectively.

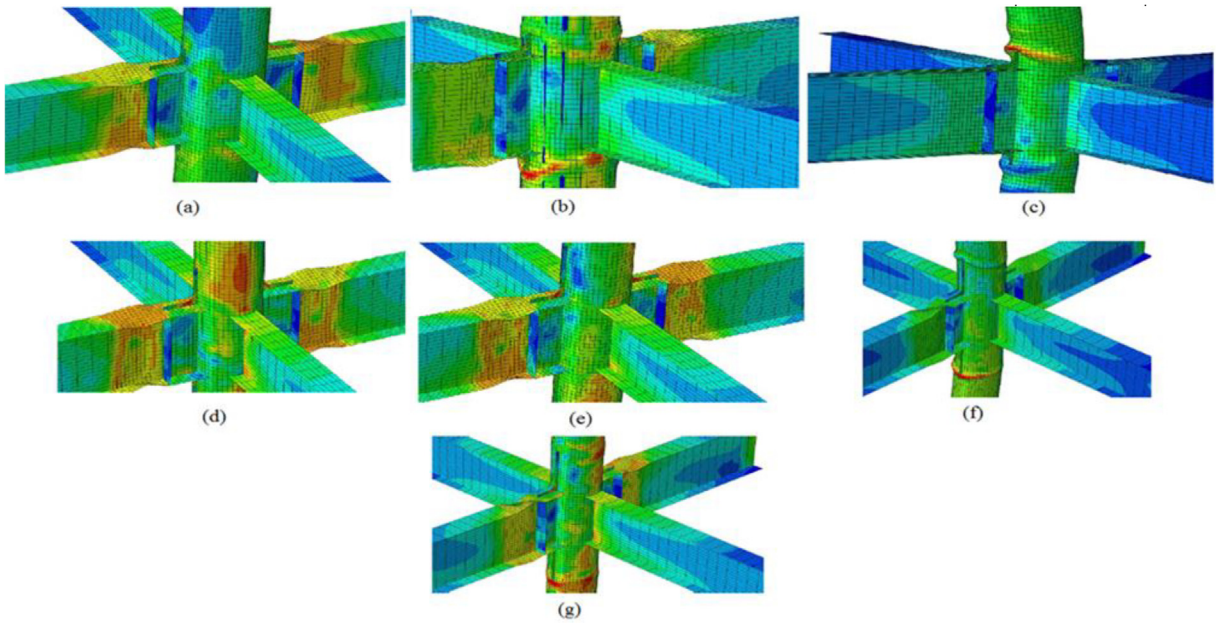

Fig. 12. Failure types of (a) FEM-11, (b) FEM-12, (c) FEM-13, (d) FEM-14, (e) FEM-15, (f) FEM-16, (g) FEM-17.

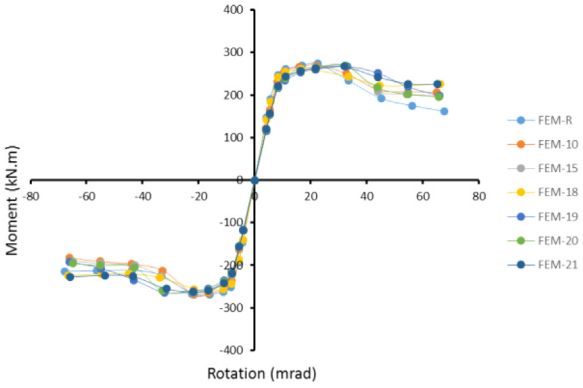

Fig. 13. The moment-rotation envelope curves of Group 3.

4.3. Effect of through rib stiffener thickness

Fig. 13 compares the moment-rotation envelope curves of Group 3. The comparison between FEM-18 and FEM-R shows that the ultimate moment of FEM-18 was 4% lower than FEM-R, which was due to thinner through rib stiffener thickness of FEM-18 compared to FEM-R. Fig. 14a shows the plastic hinges at the main beam of FEM-18 were shifted to the reinforced areas of the beam as the result of using a thinner through rib stiffener.

The comparison between the ultimate moments of FEM-19, FEM-20, and FEM-15 shows that the through rib stiffener thickness did not considerably affect the moment of these models, because the plastic hinge formed at the same locations in their main beams.

The comparison between the ultimate moments of FEM-21 and FEM-10 shows that increasing the thickness of through rib stiffeners improved the ultimate moment of FEM-10 by 3% compared to FEM-21. In addition, FEM-21 failed at the reinforced areas of its main beam due to its thinner through rib stiffener, as can be observed in Fig. 14b.

4.4. Effect of the through rib stiffener length

Fig. 15 compares the moment-rotation envelope curves of the models in Group 4. The comparison between FEM-22 and FEM-R shows that increasing the through rib stiffener length improved the ultimate moment of FEM-22 by 4% compared to FEM-R. However, the beam failure took place at the reinforced areas of the main beam of FEM-22, as shown in Fig. 16a.

The ultimate moments of FEM-23 were about 2% lower than FEM-21. Although a shorter through rib stiffener length of

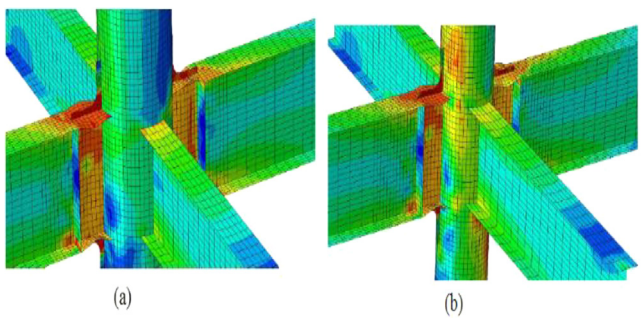

Fig. 14. Failure types of (a) FEM-18, (b) FEM-21.

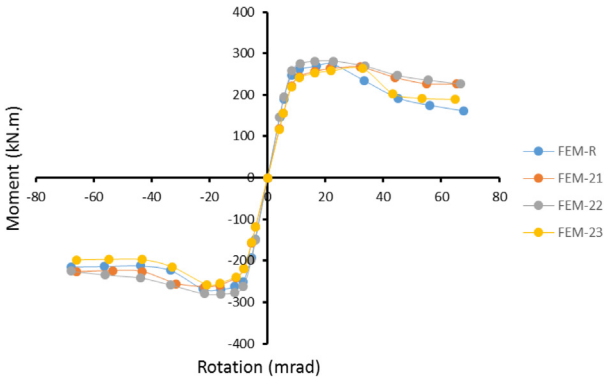

Fig. 15. The moment-rotation envelope curves of Group 4.

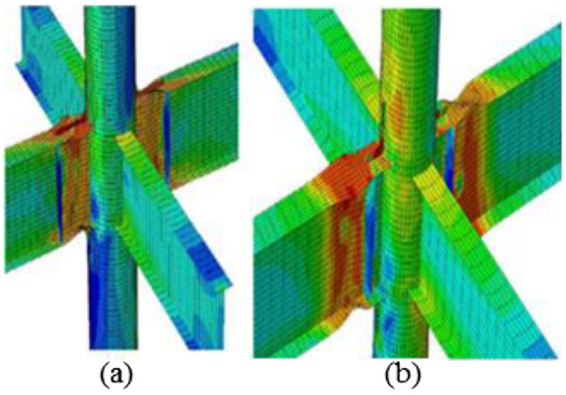

Fig. 16. Failure types of (a) FEM-22, (b) FEM-23.

FEM-23 resulted in a lower ultimate moment compared to FEM-21, the location of the plastic hinges was shifted to the unreinforced areas of the main beam, as can be seen in Fig. 16b.

5. Conclusions

This study investigated numerically the effect of different column-to-beam moment capacity ratios and the geometry of the through rib stiffener on the failure type and the ultimate moment of the connection of through rib stiffener beam to circular CFT column under cyclic loading. Based on the numerical investigation presented in this study, the following conclusions were inferred:

- The column-to-beam moment capacity ratio does not have a remarkable effect on the ultimate moment of the FE models since all the models achieved their beam plastic moment capacities. However, local bucking of the steel tube was seen in those models with the column-to-beam moment capacity ratio less than one
- The through rib stiffener height has a great effect on the failure of the steel tube. The results showed that increasing the through rib stiffener height can prevent the local buckling of the steel tube of the models with the column-to-beam moment capacity ratio greater than one. The results also showed that the ultimate moment of the connection was increased by 8% when the through rib stiffener height increased from 80 mm to 280 mm.
- The thickness and the length of the through rib stiffener have effect on the beam plastic hinge location. Using a thicker and longer through rib stiffener can improve the ultimate moment of the connection as a result of shifting the plastic hinge location away from column.

Declaration of Competing Interest

The authors declare that they have no known competing financial interests or personal relationships that could have appeared to influence the work reported in this paper.

References

[1] Y.M. Alostaz, S.P. Schneider, Analytical behavior of connections to concrete-filled steel tubes, J. Constr. Steel Res. 40 (2) (1996) 95–127.
[2] J. Wang, H. Zhang, Seismic performance assessment of blind bolted steel-concrete composite joints based on pseudo-dynamic testing, Eng. Struct. 131 (2017) 192–206. https://doi.org/https://doi.org/10.1016/j.engstruct.2016.11.011.
[3] L. Guo, J. Wang, S. Wu, L. Zhong, Experimental investigation and analytical modelling of blind bolted flush or extended end plate connections to circular CFDST columns, Eng. Struct. 192 (2019) 233–253, https://doi.org/10.1016/j.engstruct.2019.04.053.
[4] M.Z. Jeddi, N.H.R. Sulong, Pull-out performance of a novel anchor blind bolt (TubeBolt) for beam to concrete-filled tubular (CFT) column bolted connections, Thin-Walled Struct. 124 (2018) 402–414. https://doi.org/https://doi.org/10.1016/j.tws.2017.12.028
[5] B. Li, Y.-L. Yang, Y.-F. Chen, W. Cheng, L.-B. Zhang, Behavior of connections between square CFST columns and H-section steel beams, J. Constr. Steel Res. 145 (2018) 10–27. https://doi.org/https://doi.org/10.1016/j.jcsr.2018.02.005.
[6] M. Tahamouli Roudsari, S. Sohaei, M. Torkaman, A. Alizadeh, S. Safaee, A. Haghaninia, M. MohammadiMajd, Experimental investigation of I-shaped beam to circular column rigid connection with stiffened and non-stiffened channel link, J. Earthq. Eng. (2019) 1–23.
[7] Z. Lai, Z. Huang, A.H. Varma, Modeling of high-strength composite special moment frames (C-SMFs) for seismic analysis, J. Constr. Steel Res. 138 (2017) 526–537. https://doi.org/https://doi.org/10.1016/j.jcsr.2017.07.018
[8] J. Wang, H. Zhang, Z. Jiang, Seismic behavior of blind bolted end plate composite joints to CFTST columns, Thin-Walled Struct. 108 (2016) 256–269, https://doi.org/10.1016/j.tws.2016.08.013.
[9] M. Tahamouli Roudsari, S. Sohaei, M. Torkaman, S.A. Safaee, S. Tahmasebi, S. Mohammadi, M.M. Ghiasvand, Presenting a new detail for the rigid connection between I-shaped beam and concrete-filled steel tube column with stiffened channel link, Int. J. Steel Struct. 20 (2) (2020) 655–667.
[10] J. Wang, H. Wang, Cyclic experimental behavior of CFST column to steel beam frames with blind bolted connections, Int. J. Steel Struct. 18 (3) (2018) 773–792.
[11] Z. Lai, E.C. Fischer, A.H. Varma, Database and review of beam-to-column connections for seismic design of composite special moment frames, J. Struct. Eng. 145 (5) (2019) 04019023, https://doi.org/10.1061/(ASCE)ST.1943-541X.0002295.
[12] M. Zeinizadeh Jeddi, N.H. Ramli Sulong, M.M. Arabnejad Khanouki, Seismic performance of a new through rib stiffener beam connection to concrete-filled steel tubular columns: an experimental study, Eng. Struct. 131 (2017) 477–491.
[13] A. Elremaily, A. Azizinamini, Design provisions for connections between steel beams and concrete filled tube columns, J. Constr. Steel Res. 57 (9) (2001) 971–995.
[14] A. Elremaily, A. Azizinamini, Experimental behavior of steel beam to CFT column connections, J. Constr. Steel Res. 57 (10) (2001) 1099–1119.
[15] M.M.A. Khanouki, N.H. Ramli Sulong, M. Shariati, M.M. Tahir, Investigation of through beam connection to concrete filled circular steel tube (CFCST) column, J. Constr. Steel Res. 121 (2016) 144–162.
[16] E. Hosseinpour, S. Baharom, W.H. W. Badaruzzaman, A.W. Al Zand, Push-out test on the web opening shear connector for a slim-floor steel beam: experimental and analytical study, Eng. Struct. 163 (2018) 137–152.
[17] A.W. Al Zand, W.H.W. Badaruzzaman, A.A. Mutalib, S.J. Hilo, Rehabilitation and strengthening of high-strength rectangular CFST beams using a partial wrapping scheme of CFRP sheets: experimental and numerical study, Thin-Walled Struct. 114 (2017) 80–91.
[18] H. Zhao, S.K. Kunnath, Y. Yuan, Simplified nonlinear response simulation of composite steel–concrete beams and CFST columns, Eng. Struct. 32 (9) (2010) 2825–2831.
[19] Q. Zhou, H. Fu, F. Ding, X.-M. Liu, Y. Yu, L. Wang, Z. Yu, L. Luo, Seismic behavior of a new through-core connection between concrete-filled steel tubular column and composite beam, J. Constr. Steel Res. 155 (2019) 107–120. https://doi.org/https://doi.org/10.1016/j.jcsr.2018.12.002.
[20] T. Wang, T.T.C. Hsu, Nonlinear finite element analysis of concrete structures using new constitutive models, Comput. Struct. 79 (32) (2001) 2781–2791.
[21] B.S. En, 1–1. Eurocode 2: Design of concrete structures–Part 1–1: general rules and rules for buildings, Eur. Comm. Stand. (2004).
[22] D. Systèmes, Abaqus 6.10: Analysis user's manual, Provid, RI Dassault Systèmes Simulia Corp. (2010).
[23] A. Committee, Specification for structural steel buildings (ANSI/AISC 360–10), Am. Inst. Steel Constr, Chicago-Illinois, 2010.